Study of pseudoelastic systems for the design of complex passive dampers: static analysis and modeling

Adelaide Nespoli (1), Daniela Rigamonti (2), Marco Riva (3), Elena Villa (1), Francesca Passaretti (1)

1: Consiglio Nazionale delle Ricerche – Istituto di Chimica della Materia Condensata e Tecnologie per l'Energia (CNR-ICMATE) Unità di Lecco, Corso Promessi Sposi 29, 23900 Lecco (Italy)
2: Politecnico di Milano - Dipartimento di Scienze e Tecnologie Aerospaziali, via La Masa 34, 20156 Milano (Italy)
3: Istituto Nazionale di Astrofisica (INAF), via E. Bianchi 46, 23807 Merate, LC (Italy)

Corresponding author:
Adelaide Nespoli, MSc
telephone: +39 0341 499181
fax: +39 0341 499 214
e-mail: adelaide.nespoli@cnr.it

Abstract
This work presents an experimental and numerical analysis of several parallel systems of NiTi pseudoelastic wires. Standard tensile tests were accomplished to evaluate the global damping capacity, the energy dissipated per cycle and the maximum attenuated force in a static condition. Besides, a numerical model was implemented to predict the damping response of more complex pseudoelastic arrangements. It was found a damping capacity upper limit of 0.09 regardless the number and the length of the NiTi components. In addition, it was found that the energy dissipated per cycle is related to the strain and to the number of the NiTi components; furthermore, the system composed of NiTi wires with different length allows for an elastic region that is related to the numbers of wires and that presents a modulation of the stiffness. Finally, the proposed numerical model allows a precise design of complex pseudoelastic combinations as it is able to represent the Rhombohedral characteristic.

keywords
shape memory alloy; pseudoelasticity; damping; rhombohedral phase; NiTi modeling

1. Introduction

Equi-atomic NiTi alloys are known for their unique and excellent mechanical properties related to the high strain recovery (shape memory effect) and to the peculiar pseudoelastic behavior. At the base of these two mechanical responses, there is a first order thermo-elastic martensitic transformation between two different solid phases, martensite with monoclinic crystalline structure, and austenite with body centered cubic lattice, that go into a recoverable displacive non-diffusional process [1 - 6].

Pseudoelasticity occurs when the material is in the austenite state, that is to say when the operating temperature is higher than Af (austenite finishing temperature), and in this case, martensite nucleates from austenite at a constant stress (stress induced martensite, SIM). In the stress–strain diagram (see Figure 1 as an example), pseudoelasticity appears as a flag shaped curve, and, in particular stress conditions, a recoverable maximum strain of 8 - 10% can be associated to one single load/unload cycle [1, 3].

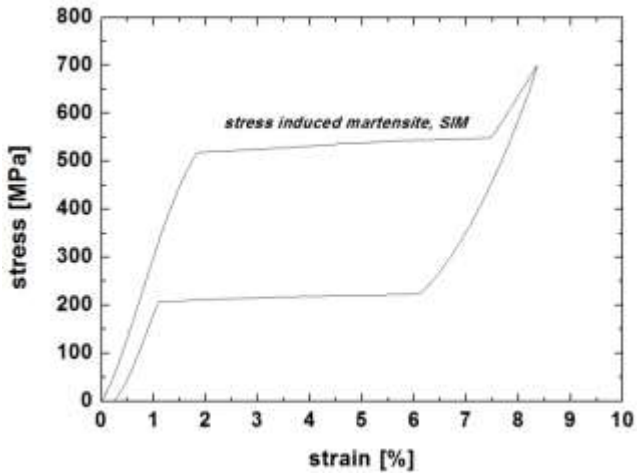

Figure 1. Typical flag-shaped pseudoelastic tensile curve of a NiTi sample above Af temperature [CNR-ICMATE Lecco Unit didactic document].

According to the stress-strain diagram of Figure 1, the pseudoelastic loading path starts with a linear elastic response that can be used to recover low variations of strain at high forces. This elastic behavior is followed by a second marked segment that is characterized by an almost constant stress plateau, in which martensite is induced by stress (SIM). During this step, the martensite variants with the maximum resolved shear stress among the possible 24 variants, are preferentially formed: throughout the plateau, the high mobility of the interfaces of the martensite variants minimizes the strain energy allowing high deformation at quite constant stress. The SIM plateau is therefore used to avoid a linear increasing of the load during high changes of strain until the complete transformation of the material into SIM. Then, the elastic deformation of the SIM completes the standard pseudoelastic loading path. During unloading, the strain is first recovered through the elastic regaining of martensite and the martensite-to-austenite transformation at constant stress and finally, by the elastic recovery of austenite. Through this hysteretic mechanical cycle, the SMA is capable to passively dissipate a large amount of energy during one load/unload cycle and it allows to damp the strain recovery of an associated structure through a soft return to the rest position [7-11].

Passive pseudoelastic dampers have attracted much interest in the last decades especially in civil engineering. In this field, the high dissipated energy associated with a series of load/unload cycles of a pseudoelastic shape memory element is used to damp or prevent the oscillations of a physical system. In this context, the pseudoelastic component acts as isolator and it works in the control and recovery of the deformation that is imposed by the external event. There are two main applications of pseudoelastic dampers in civil engineering: the mitigation of the oscillations in structures induced by earthquakes, and the reduction of the oscillations amplitude in stayed cables under action of rain, wind or traffic. Torra et al. [12] defined appropriate requirements for a pseudoelastic civil damper. As regards earthquake, the device has to work at least 1 000 working cycle with an oscillation frequency of 1Hz. These requirements increase for the stayed cable case, for which the frequency may arrive up to 18Hz with the working cycles that can increase up to 4 million cycles.

Besides, there are many other fields in which damping of vibration is mandatory for human security, and some examples in the automotive, biomedical an aerospace fields are here presented. i) The vehicle suspension has to minimize the transfer function of vibration from the rough road to the vehicle's body, over the entire concerned range of frequencies (0.1–100 Hz) for all the vehicle life [13]; ii) tremor is one of the most common neurological disorders among adults, and it is clinically described as a rhythmical, involuntary oscillatory movement of a body part produced by reciprocally innervated antagonist muscles, and it typically manifests at a frequency in the range of 3 – 12 Hz with a unlimited duration [14]; iii) aircraft pilot comfort requires continuous work in decreasing vibrations in the seat that is usually affected by vibrations in the frequency range of 1 Hz to 200 Hz [15].

Some ways to improve the damping capacity of a massive damper with a pseudoelastic core are shown in the works of Indirli et al. [16] and Ren et al. [17]. Indirli presented a multi-plateau self-balance SMA device (SMAD) that shows different stress plateaux. According to Indirli's study, the pseudoelastic response of a SMAD results in a multi force level at which a single plateau occurs. Previously, Ren et al. presented an interesting study on the damping response of a re-centering damper made of two functional groups of superelastic strands that differentiate one with the other by the pre-tensioning state.

On the base of Indirli's and Ren's studies, in this work new ways to modulate and improve the damping response of pseudoelastic materials are presented; in detail, some articulated pseudoelastic systems are evaluated through the measure of the damping capacity, the dissipated energy and the maximum force during mechanical cyclic tests in a static condition. On the base of the experimental results of several simplified systems, a complex re-centering and bi-directional arrangement is presented and tested. At the same time, a numerical simulation was implemented to predict the damping response of more complex devices. At present, a significant number of models exists mainly for three purposes. The first one is to understand the underlying physics and mechanisms that cause the observed effects: this helps to explain the experimental phenomena and it can be fulfilled with micromechanical models. Some examples are Fischer and Tanaka [18], Raniecki *et al.* [19], Bernardini [20]. The other two purposes are to identify the material properties or processing parameters that can yield the desired effects in terms of shape memory effect, superelasticity, two-way-shape memory effect, etc. (material development) and to predict the material response in conjunction with a smart device or a system that is under investigation (application development). The last two purposes are consequence of the spread of the applications of SMA and of the resulting need for a design tool and they are the ones for which macromechanical models are the most

suitable. Macromechanical models are mainly divided in two categories: phenomenological and thermodynamic. Phenomenological models draw heavily on the observed exhibition of the functional properties of the material and are suitable for engineering practice, because they make use of measurable quantities as parameters and are often relatively simple. They are sometimes also called 'state models' because use a Stress-Temperature phase diagram to identify appropriate transformation bands [21 - 24]. On the other hand, thermodynamic models are based on the free energy description of the material behavior [25 – 27]. The model used in this work is an uniaxial phenomenological model based on the one by Zhu and Zhang [28], which is in turn an elaboration of that by Tanaka [21].

To maximize the pseudoelastic hysteretical mechanical curve, it was decided to use a material that is in the rhomboedral phase (hereinafter called R-phase) at room temperature. Starting with this microstructural condition the pseudoelastic curve has a wider mechanical hysteresis with respect to a conventional pseudoelastic material that is normally in the austenitic initial state; however, starting from a R-phase condition rather low forces can be reached during loading with respect to the austenitic state [29]. In terms of modeling, the R-phase is still poorly investigated [30, 31], because of two main motivations. The first one is that the R-phase, together with a calorimetric relevance and the utility in damping applications, contributes mechanically only for strain below 1%, up to an order of magnitude less than those of the SIM, and for stress below 200-250 MPa. The second reason is that the definition of the R-phase is a problem in outlining the phase diagram, which is an essential first step to characterize this type of phenomenological models, because of the lack of evidence indicating what happening exactly during the stress-induced R-phase formation. To define the phase diagram, there is the need to understand the behavior of the R-phase at different temperatures. It is analyzed for instance in [32] mainly for temperatures below the one of the Rhombohedral finish transformation, RfC, in [29] and especially in [33], which focuses in detail on the temperatures in the transformation band austenite-to-rhombhoedral, AtoR, that are those of our interest.

Therefore, this work focuses on the study of the mechanical response of some parallel systems based on pseudoelastic NiTi wires that were prepared to be in the R-phase at room temperature; experimentation and modeling allow then the design of complex pseudoelastic systems. To understand the mechanical response of the considered pseudoelastic arrangements, the experimentation and the modeling were both accomplished in a quasi-static configuration.

2. Materials and Methods

2.1 Experimental tests

All devices are based on a commercial NiTi wire (SmartFlex, from Saes Getters, Italy) with 1.2mm diameter and annealed at 450°C for 10 minutes (followed by quench in water at room temperature).

Differential scanning calorimetry (DSC, Q100 TA Instruments) equipped with a liquid nitrogen cooling system was used to evaluate the phase transformation temperatures of the wire after annealing. The temperature range for the DSC measurement was from -120 °C to 80 °C at the controlled heating/cooling rate of 10 °C/min.

Quasi-static tensile tests were accomplished to evaluate the mechanical response of the single NiTi wire, of the basic pseudoelastic systems (BPS) and of a final articulated device. These tests were made by a MTS 2/M thermo-mechanical testing machine (MTS Systems) equipped with a thermal chamber, at 23°C constant temperature and at the controlled deformation rate of 1%/min (0.5mm/min).

The BPS consists of two NiTi wires arranged in parallel tensile configuration, and the following combinations were considered:

1. parallel of two NiTi wires having the same length. In this case, the two NiTi wires perform the same absolute stroke and the same strain as the resulting BPS. Tests were performed at different strain: 2%, 3%, 4% and 5%.
2. parallel of two NiTi wires having different length (L_1=60mm, L2=1.5L_1). In this case, the two NiTi wires perform the same absolute stroke as the resulting BPS but with own strains. The considered absolute strokes and the strain referred to the two NiTi wires during tensile tests are reported in Table 1. During these tests, the 1%/min deformation rate was calculated on the length of the shortest wire (i.e. 0.6mm/min).

BPS absolute stroke [mm]	**wire 1 maximum strain [%]**	**wire 2 maximum strain [%]**
0.9	1.5	1
1.8	3	2
2.7	4.5	3
3.6	6	4

Table 1. Absolute stroke of BPS and maximum strains of the two NiTi wires during tensile tests.

During the mechanical tests of BPS, the NiTi wires were fixed on two holders as the ones reported in Figure 2, and the change in length of the BPS was evaluated by a clip-on extensometer (MTS Systems). Figure 3 reports a schematization of the two configurations that were considered for the characterization of the BPS. On the base of the two combinations of the BPS testing, an articulated device was designed, realized and tested via the MTS machine.

Moreover, the damping capacity was evaluated through the loss factor calculation. According to published literature, the loss factor is the most suitable index for describing the damping capacity of materials and it was originally introduced as a measure of the intrinsic damping of viscoelastic materials. In this context, it is defined as the ratio between the real (loss modulus, $\boldsymbol{E''}$) and the imaginary (storage modulus, $\boldsymbol{E'}$) parts of the elastic complex modulus [34]:

$$\eta = \frac{E''}{E'} = \tan\delta \quad (1)$$

Alternatively, a definition in terms of energy concepts can be used:

$$\eta = \frac{W_d}{2\pi W_e} \quad (2)$$

where $\frac{W_d}{2\pi}$ is the energy dissipation per cycle per radian, and W_e is the stored energy during loading. With this definition, the loss factor represents the damping as a global characteristic [35] . In this work, the loss factor was evaluated from the tensile curves according to this latter definition.

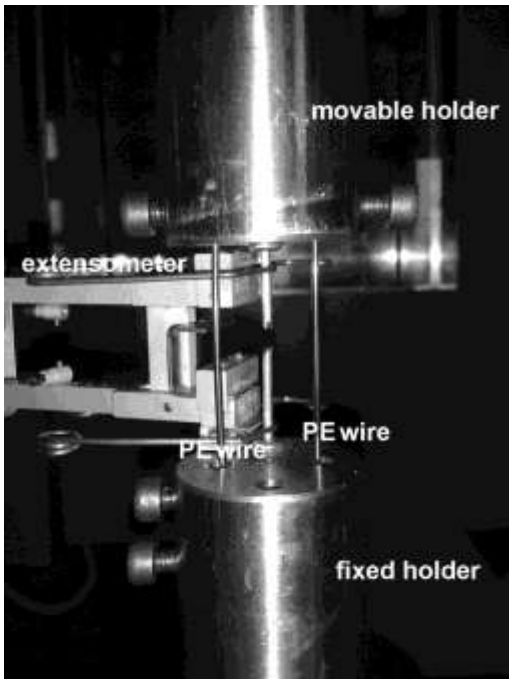

Figure 2. Experimental setup during tensile tests of BPS.

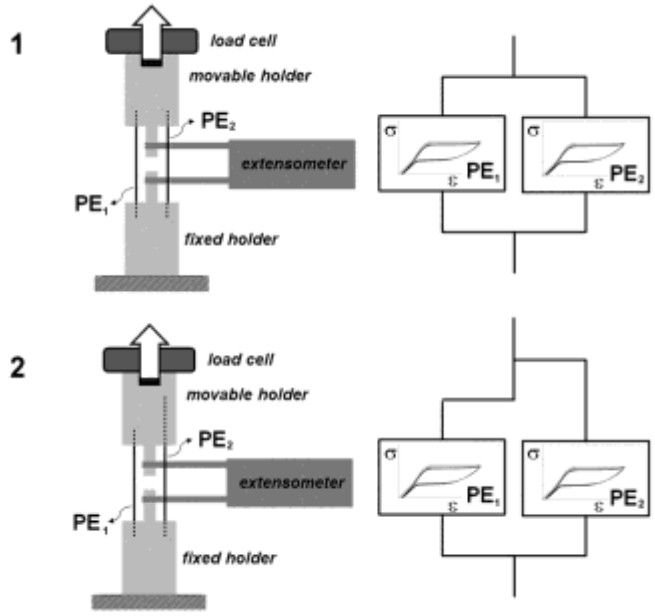

Figure 3. Schematic representation of the experimental procedure used to evaluate the global damping capacity of the articulate NiTi systems (1: parallel of two NiTi wires, PE_1 and PE_2, with the same length, 2: parallel of two NiTi wires, PE_1 and PE_2, with different length).

2.2 Model characteristics and implementation

Due to the nature of the stress-induced martensitic transformation, to obtain maximal recoverable deformation, the great number of applications of shape memory alloys is often one-dimensional, as the configuration used in this work. In view of this, it was decided to implement a uniaxial phenomenological model starting from the one by Zhu and Zhang [28]. It consists in a mechanical law governing the stress-strain behavior, an energy balance equation that reflects the rate-dependent thermal effect and a transformation kinetics law that describes the evolution of the phase fraction as a function of stress with a sigmoidal law.

As previously reported, a material with an R-phase microstructural state has been chosen. Originally, the model by Zhu and Zhang does not consider such phase, so it has been modified to include it. First, the hypothesis of sequential order of the phase transformations was formed; this means that the transition of volume fraction always takes place between two phases, generating four transformation bands (AtoR, RtoM, MtoR, RtoA, where A, R and M are the austenite, rhombohedral and martensite phases) of which only one at a time is in progression. Having different Clausius-Clapeyron coefficients, these bands can intersect one with the other. When this happens, in order to maintain the first hypothesis, it was considered that the transformations that do not include the R-phase take precedence. The second hypothesis is that the rhombohedral transformation has the same thermodynamics of the martensitic one, but different kinetics. This will be thoroughly explained in Section 3.1.

The thermodynamics base of the model is the free-energy density of superelastic SMA that is assumed here to be in the Helmholtz formulation:

$$\psi = \frac{E(\xi)}{2\rho_0}(\varepsilon - \varepsilon_L\xi)^2 + \frac{L_h}{T_{cr}}(T - T_{cr})\xi - C_pT\,ln\left(\frac{T}{T_0}\right) \quad (3)$$

The dependence of the Young modulus E from the martensite fraction is taken in the Voigt form:

$$E(\xi) = E_A\xi_A + E_M\xi_M + E_R\xi_R \quad (4)$$

The material constants L_h, C_p and T_{cr} are the latent transformation heat, the specific heat and the transformation temperature of the material. The variable ε_L is the maximum transformation strain, i.e. a measure of the maximum deformation obtainable only by the detwinning of the multiple-variant martensite and it is also a material constant, taken equal to 7% for martensite and 0.7% for R-phase. In the expression of the strain and consequently in all the derivative of the Helmholtz energy with respect to (T, ε, ξ), the thermal expansion is omitted, because its effect is negligible. If it is to be added, the strain has to become $\varepsilon = \varepsilon - \varepsilon_L\xi - \alpha\Delta T$ and all the equations have to be derived again.
Deriving with respect to the state variables $(\sigma, \varepsilon, \xi)$ and the time, and applying the energy balance equation and the Clausius-Duhem inequality, the expressions of the rate of the variables are obtained and can be implemented in the integration algorithm.

$$\dot{\sigma} = E(\xi)\varepsilon + \left(-\varepsilon_L \cdot E(\xi) + (E_M - E_A)(\varepsilon - \varepsilon_L\xi)\right)\dot{\xi} \quad (5)$$

$$\dot{T} = \dot{\xi} * [\varepsilon_L E(\xi)(\varepsilon - \varepsilon_L\xi) - 0.5(E_M - E_A)(\varepsilon - \varepsilon_L\xi)^2 + \rho_0 L_h]/\rho_0 C_p - k(T - T_0)/V\rho_0 C_p \quad (6)$$

Different transformation kinetics rules have been proposed to describe the evolution of the phase volumetric fraction of SMAs, however, according to [28], using the sigmoid function reduces the sharp transition at the critical stress, resembling more closely experimental results. The evolution of phase fraction is expressed as

$$\dot{\xi} = (1 - \xi_X)\left[-a_X\left(\dot{T} - \dot{\sigma}/C_X\right)\right] \cdot g[-a_X(T - T_{PX} - \sigma/C_X)] \quad (7)$$

which is the derivative form of

$$\xi = \xi_X + (1 - \xi_X) \cdot sig[-a_X(T - T_{PX} - \sigma/C_X)]\,, \quad (8)$$

with:

$$a_X = \ln(P)\,/|T_{SX} - T_{FX}| \quad (9)$$

Equations 7, 8 and 9 have the same formulation for each transformation and the subscript 'X' is used in to indicate the product phase of the one that is occurring. The argument of the logarithm P is a

phenomenological parameter, which can be modified to better accommodate the experimental behavior. In this case, it is taken 100.000 for RtoM and MtoR transformations and 800 and 1000 for AtoR and RtoA respectively, as explained also in Section 3.1. The model account also for self-heating effects, due to the heat released/absorbed during transformation, but for the simulation of the temperature change to be reliable, the convective exchange coefficient has to be correctly evaluated. This is particularly important if performing a cyclic loading, when the effective test temperature changes if the loading rate is high [28].
The model has been implemented in a Matlab® routine, which integrates the equations using a fourth order Runge-Kutta algorithm. At each step of integration, the ongoing transformation is determined depending on the value of the state variables (stress and temperature) and on the direction of progress of their ratios in the phase diagram. Hence, the equations for the ongoing transformation are solved and then integrated.
The AtoR and backward transformations occur only at strains below 0.7%, contributing to the total deformation with a transformation strain equal to only 1/10 of the one involving martensite. In consideration of this, for the wires or BPS with strain greater than 3%, only the transformations involving martensite are supposed to exist. In all the other cases, the rhombohedral transformation cannot be ignored and then the routine is modified to include this aspect. In particular, the thermodynamic of the transformations is maintained, but the phase diagram is modified to include the other two transformation bands.

3. Results

3.1 Model validation

To tune and validate the model and to define the transformation bands, i.e. the phase diagram, the experimental tests on single wires were analyzed together with the DSC curve. Figure 4 reports the DSC curve of the material where the peaks of the R-phase [36] can be observed, and it can be also seen that at room temperature (RT) the material is in the AtoR region below the peak temperature. According with [29] and [33], in this range the mechanical response of the AtoR transformation does not displays a plateau, but rather a curvature that causes a gradual increase of slope. This condition is modeled modifying the kinetics: using the value 800 as argument of the logarithm in the sigmoid law, this results in a very rapid transformation, for which the plateau is not developed, but there is only the final part of the sigmoid (i.e. the curve with the concavity upwards). This approach, which is possible because the phenomenological models allow calibrating the kinematics by the observed behavior, proves to be valid because there is good accordance with all experimental data. As an example, two tests at low strains are reported in Figure 5 (less than 1% strain) and Figure 6 (1.8% strain): in the first example (Figure 5), the only transformation observable is the AtoR followed by the backward RtoA, while in the second test (Figure 6), all transformations are present as indicated by the superimposed circled points.

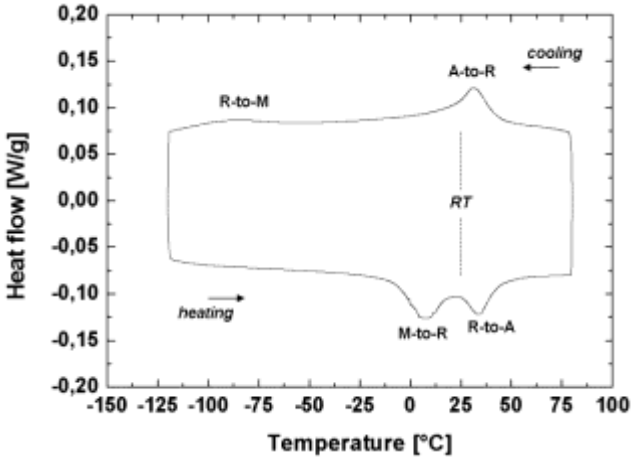

Figure 4. DSC curve of NiTi wire thermal treated at 450°C for 10 minutes (A: austenite phase; R: rhombohedral phase; M: martensite phase; RT: room temperature).

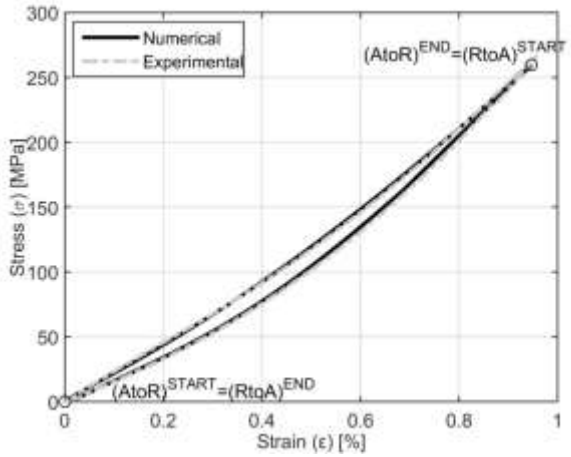

Figure 5. Stress-strain tensile behavior for a NiTi wire stretch up to 1% strain. The curvature is due only to AtoR and backward (RtoA) transformations.

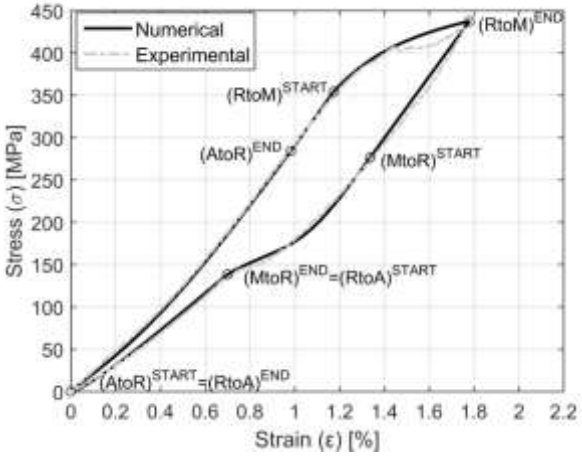

Figure 6. Stress-strain tensile behavior for a NiTi wire stretch up to 1.8% strain. The circles indicate the starting and ending points of the transformations.

The other values used in the model are derived from the experimental thermo-mechanical characterization: the latent heats of the four transformations (values in Table 2) and the specific heat (449 J/kg/K)) from DSC analysis, while the elastic moduli from mechanical tests. In particular, to determine E_A and E_M, a tensile test at 50°C (above Af) has been performed and gives the values of 51 GPa and 20 GPa respectively in the two elastic regions before and after the transformation plateau. The R-phase elastic modulus is more difficult to determine because of the uncertainty of the temperature at which perform the tensile test that shows a pure rhombohedral elastic region, so its value has been chosen equal to 28 GPa to better accommodate the experimental behavior during transformation.

Tensile tests at different temperatures allow obtaining the Clausius-Clapeyron coefficients of the transformations RtoM and MtoR, considering the stresses at which their respective plateaux start. A linear regression between those stresses defines the lines of RtoM and MtoR start, while the finish lines are taken parallel to the start ones and intersecting at zero stress the respective transformation finish temperature. The stress at which the initial curve region of the loading path ends identifies the AtoR finish. In this case, the interpolation between these stresses at different temperatures, gives the AtoR finish line, while the starting one is parallel. To define the RtoA transformation, another consideration has to be done. In the test at 1% strain (Figure 5), no elastic region is present in the unloading path and then the stress of RtoA start is at least 250 MPa. Nevertheless, considering the test at 1.8% (Figure 6), this implies that this value is greater than the stress of MtoR end. The explanation is that RtoA triggers only for deformations less than R-phase maximum transformation strain (0.7%). Therefore, together with the phase diagram, the strain value has to be considered as a third 'state variable' in addition to temperature and stress and as such it has been considered in the simulations, to determine the beginning of the RtoA transformation. From these considerations, the straight lines of the transformation bands in the phase diagram are identified and the coefficients are reported in Table 2. The resulting phase diagram as well as the stress-temperature path during test is reported in Figure 7. In particular, Figure 7a reports all the transformation lines (two for each transformation: start and finish), that can be distinguished looking at the transformation temperatures labels on Temperature axis. Black lines are for the two major transformations, gray ones for the two R-phase transformations, while solid lines are for transformations occurring in loading (cooling if looking at DSC) and dotted lines for that taking place in unloading (heating). The thin vertical line is the transformation path at the temperature of the tests (23°C). Proceeding on the line while increasing load, transformations AtoR and then RtoM are triggered when the load value is comprised in the corresponding transformation bands (solid lines). Same thing happens when following the line while unloading: the triggered transformations are MtoR first and then RtoA, passing through the bands with dotted lines. Figure 7b shows that path in the close neighborhood of the test temperature for the same test of Figure 8b. The four transformations bulges and lines are labeled, while the gray solid lines are the elastic zones between transformations.

Transformation	Coefficient (MPa/K)	Maximum transformation strain (%)	Sigmoid logarithm argument	Latent Heat (J/kg)
AtoR	5.5	0.7	800	7500
RtoM	4.8	7	100000	1860
MtoR	6.5	7	100000	6440
RtoA	6.8	0.7	1000	4380

Table 2. Value of the slope of the straight lines of the transformation bands in the phase diagram and of the maximum strains.

The phase diagram would include, according with [32], a band with a slope coefficient negative or null, which identifies the detwinning of the R-phase at temperatures below RfC in analogy with the martensitic transformation. In the cases treated in this paper, a simplified diagram with only the straight transformation bands was considered because the tests are never performed in that temperature range. However, it is worth underlining the importance to characterize the material and to define the correct diagram (i.e. the stress-temperature conditions for each transformation), basing on design conditions, otherwise the modeling results cannot be reliable.

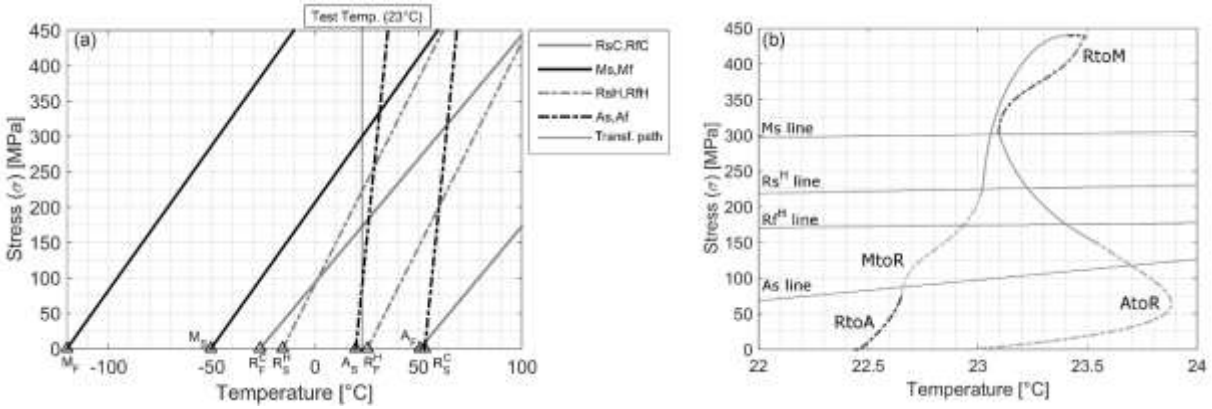

Figure 7. Phase diagram with the transformation bands (a) and zoom of the stress-temperature path (b) of the tensile behavior for the NiTi wire up to 4%. In Figure (a), black lines are for the two major transformations, gray ones for the two R-phase transformations; while solid lines are for transformations occurring in loading (cooling if looking at DSC) and dotted lines for that taking place in unloading (heating). The thin vertical line is the transformation path at the temperature of the tests (23°C).

Increasing the maximum test strain, the curvature due to the rhombohedral transformation does not change, but it becomes less relevant than the SIM contribution. For this reason, in the tests with strain less than 3% the rhombohedral transformation is considered; while in the other cases, the elastic part has a single slope, whose elastic modulus is equal to that of the purely rhombohedral phase: 28 GPa. The area of hysteresis and the reached maximum load are simulated with good accordance in both cases. The differences due to the presence of the R-phase are that the curvature of the initial loading path is better fitted and the loop is closed in the end of the unloading path (Figure 8). In that region (unloading curve, below 0.7% strain), the simulation without R-phase has a linear purely elastic segment that does not fully represent the experimental behavior of the wire and leave an amount of unrecovered strain that is associated with R-phase not recovered into austenite.

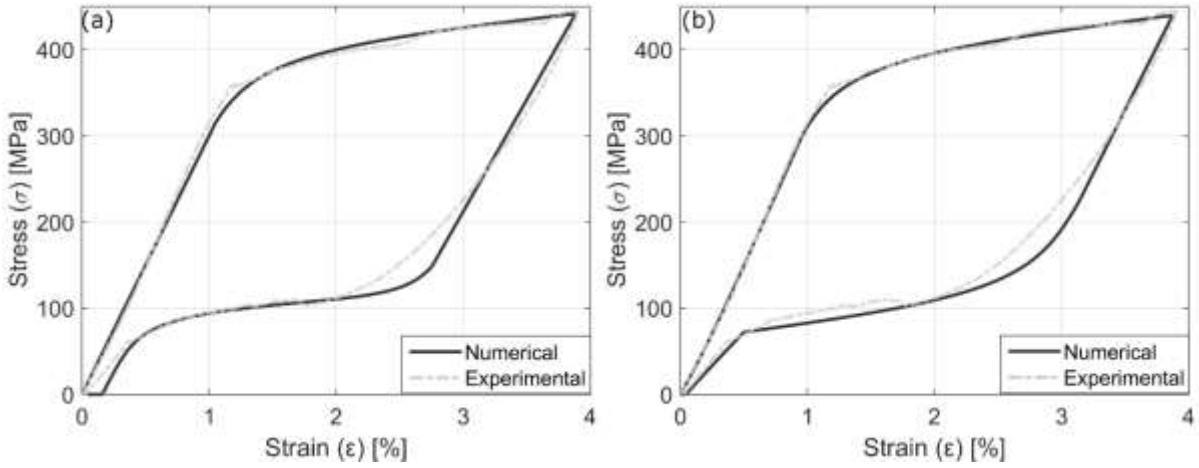

Figure 8. Stress-strain tensile behavior for a NiTi wire stretch up to 4% strain, (a) without R-phase modeling and (b) with R-phase.

3.2 Parallel system of NiTi wires with the same length

Figure 9 shows the experimental (black dashed line) and modeling (black solid line) tensile curves of the BPS composed of two NiTi wires with the same length. Experiments were made at four different maximum strains (2, 3, 4, and 5 %) and, by comparison, the experimental response of a single NiTi wire (grey solid line) is reported as well. Figure 10 reports the damping capacity (η) and maximum expressed recovery force (F_{max}) of BPS and of the single NiTi wire. From the experimental curves, it can be observed that the loading and the unloading plateaux of the BPS start at the same strains as the ones of the single NiTi wire and they occur at the double of the force of the single wire; it means that the BPS acts as a regular parallel system. Furthermore, from data reported in Figure 10, it can be seen that the global damping capacity of BPS is very similar to that of the single NiTi wire. The numerical simulation confirms the experimental result that this case is equivalent to the superposition of two identical wires, with the same strain of transformation start and the same displacement control law. Therefore, in this case, the forces cannot do other than duplicating (i.e. adding one with the other) confirming the experimental observations.

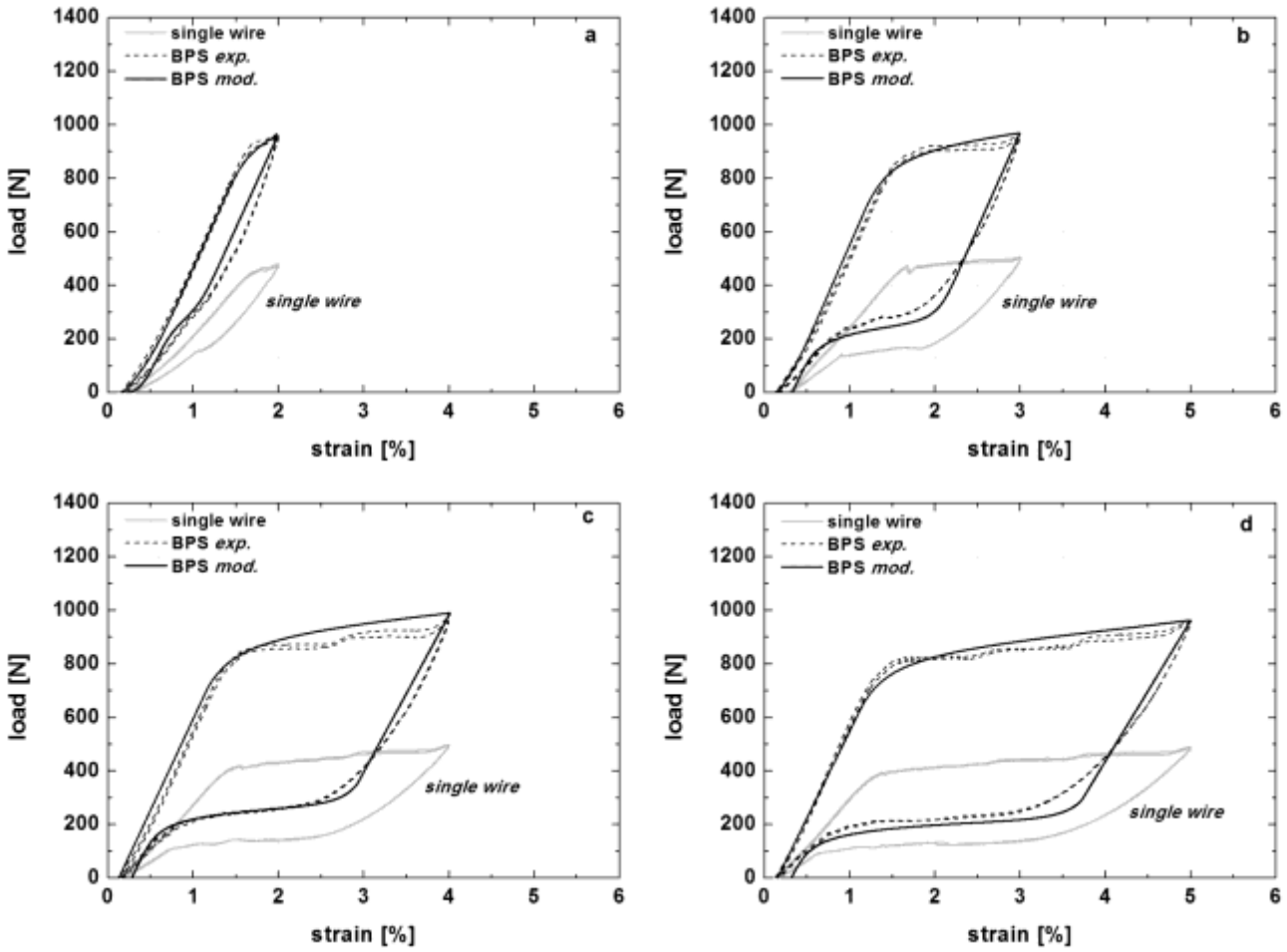

Figure 9. Force *vs.* strain of a single NiTi wire (grey solid line) and of a BPS composed of two NiTi wires with the same length (dashed solid line: experimental curve; black solid line: model curve) at different maximum strain: a: 2%; b: 3%; c: 4%; d: 5%.

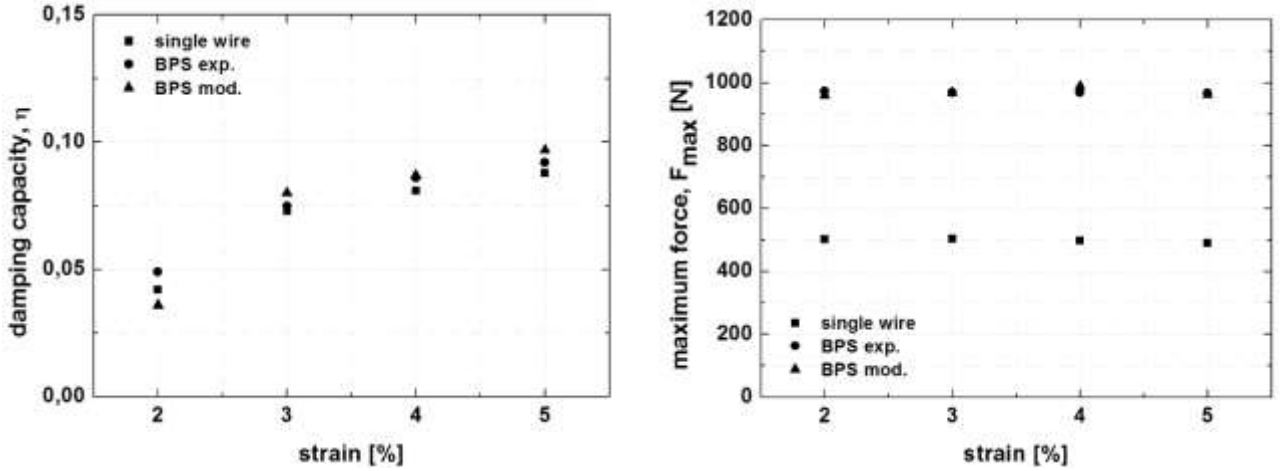

Figure 10. Damping capacity (η) and maximum force (F_{max}) of a single NiTi wire and of a BPS composed of two NiTi wires with same length (BPS exp.: experimental measurement; BPS mod.: modeling). In experimentations, η was evaluated on the second mechanical cycle while F_{max} is the mean value of three mechanical cycles.

3.3 Parallel system of PE wires with different length

In this section, the mechanical response of a BPS composed of two NiTi wires with different length is studied. Due to the different lengths, the two NiTi wires perform the same absolute stroke but different strains when work together. Figure 11 reports the experimental and modeling response of this BPS and the performance of the two single NiTi components. All the tests were performed according to the data described in Table 1, and because of the impossibility to plot all the curves as a function of strain (due to the two different lengths); all measures are reported as a function of the absolute stroke. Figure 12 reports the damping capacity (η) and maximum force (F_{max}) of BPS and the NiTi components.

To understand these experimental results, a mechanical evaluation should be done: as a matter of fact, when two pseudoelastic wires with different length work jointly, there is the overlapping of the corresponding flag-shaped curves with SIM starting at two different values of the absolute stroke. Initially the two wires are both in their elastic region (e.g. below 0.62 mm in Figure 13). When the shortest wire goes into SIM plateau, the longest one is still in its elastic region, so the resulting load trend shows a slope change and the elastic modulus of BPS decreases (stroke from 0.62 to 0.93 mm in Figure 13). When the longest wire starts transforming into the stress-induced martensite too, the BPS shows a plateau that is located at a force level equal to the sum of the plateaux of the two single pseudoelastic wires (Figure 11, approximately 500 N for a single wire and 1000 N for the BPS). From here onwards, both the two wires transform into stress-induced martensite (above 0.93 mm in Figure 13) but, at the end of loading, the percentage of detwinned martensite in the two wires is different. It can be also observed that this mechanical shift allows BPS to have damping capacity between that of the two NiTi components. Because the slope change is not so evident, to highlight it better, the first derivative of the total load (for loading only) is calculated for the simulation of the sample d (4%+6%) and it is reported in Figure 13. The derivative helps also to identify the two different strokes at which the SIM transformation starts, because they correspond to two clear falls in the derivative itself. In the example used in Figure 13, they are equal to 0.6193 mm and 0.9286 mm, both equivalent to 1.03%. The model again predicts well the experimental behavior (see Figure 11, 12 and 13); in fact, the two point of discontinuity highlighted by the derivative and due to the different strokes at which the SIM of the two single wires starts match those detectable in experimental tests.

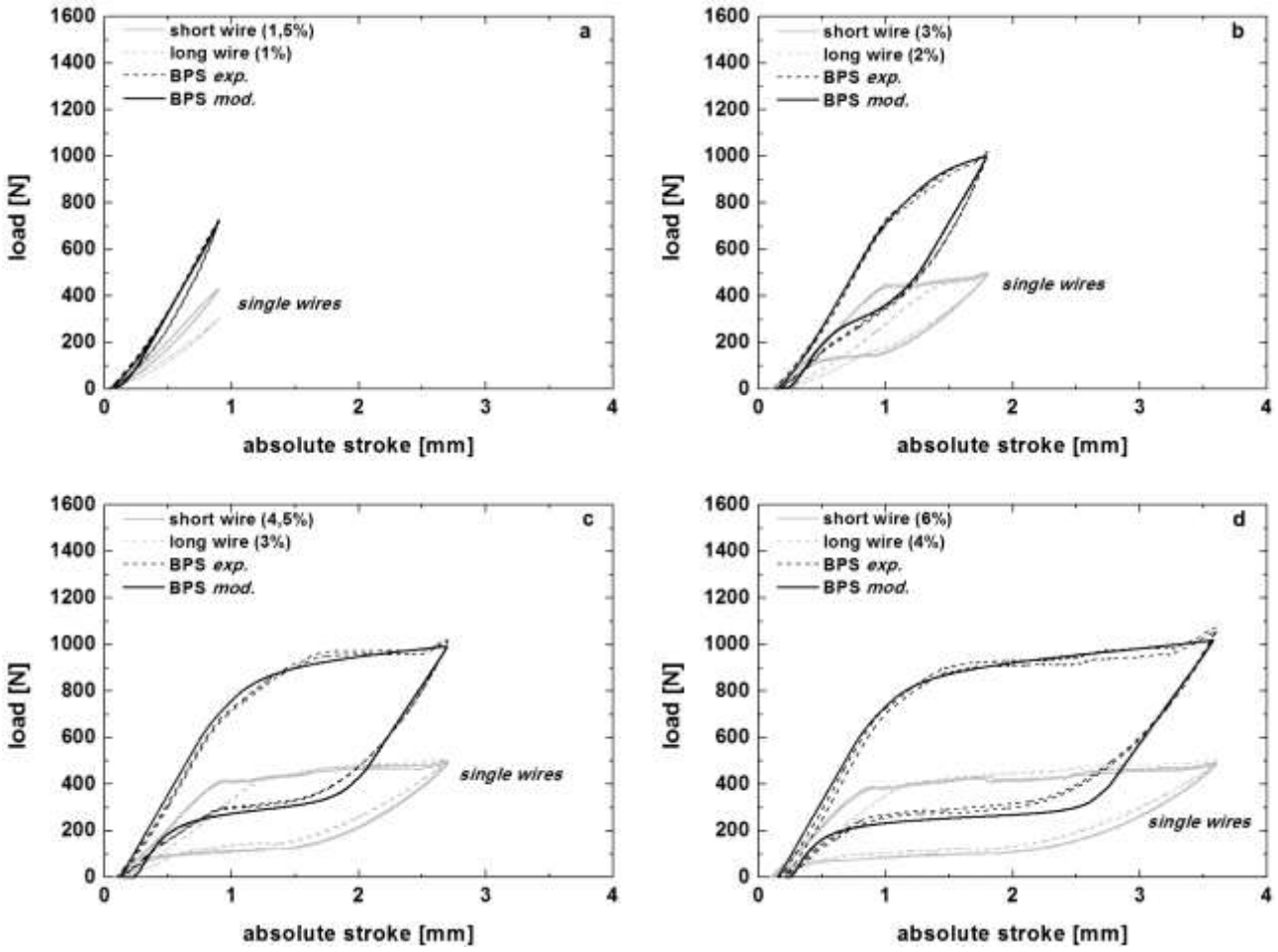

Figure 11. Force *vs.* absolute stroke of a BPS composed of two NiTi wires with different length (black dashed line: experimental curve; black solid line: model curve) and of two single wires that performed at different strain (grey dashed line: experimental curve of the long wire; grey solid line: experimental curve of the short wire).

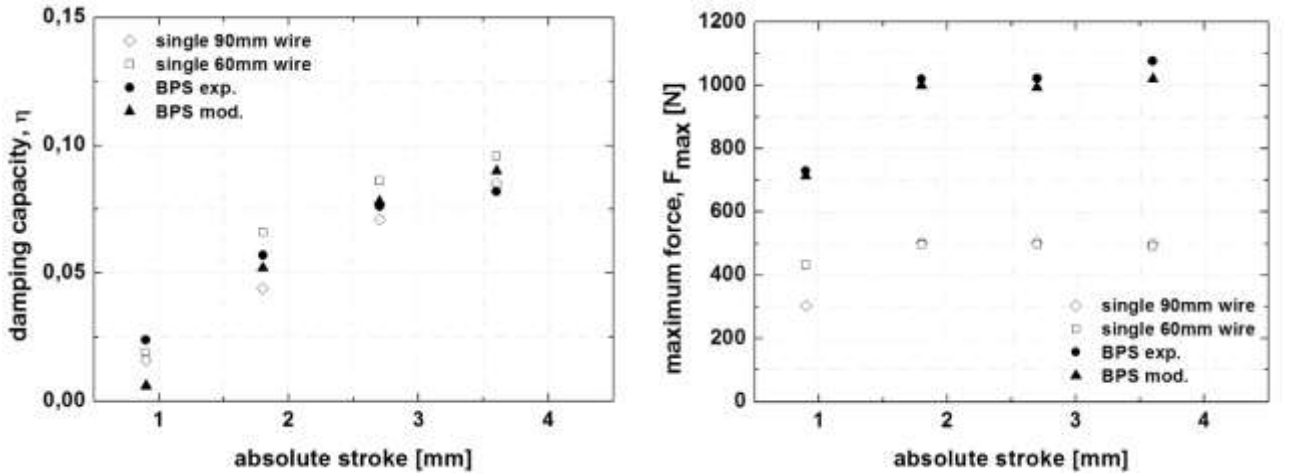

Figure 12. Damping capacity (η) and maximum force (F_{max}) of single NiTi wires and of a BPS composed of two NiTi wires with different length (BPS exp.: experimental measurement; BPS mod.: modeling). In experimentations, η was evaluated on the second mechanical cycle while F_{max} is the mean value of three mechanical cycles.

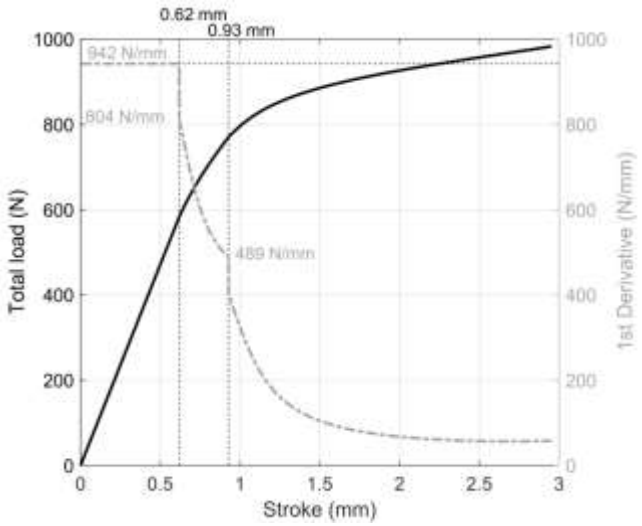

Figure 13. Total load (solid line) and its first derivative (dashed line) vs. stroke for the loading path for the simulation of the sample d (4%+6%).

3.4 Complex combination of BPS

The pseudoelastic configurations previously presented have the principal capability to promote the re-centering, that is to say that the systems are able to regain the imposed deformation with a complete recovery of the initial shape and with the concurrent dissipation of high mechanical energy. According to these setups, a new system is now presented. The device is mainly composed of two groups of pseudoelastic wires that work in a parallel configuration: the wires of the first group have length l_1, while the wires of the second group have length $l_2 < l_1$, and the parallel configuration of group 1 and group 2 defines the main system. In order to promote the bi-directionality, a system symmetrical to the main one is prepared and mounted on to the device; the resulting apparatus is therefore designed to reproduce the experimental conditions (NiTi wires with the same length and NiTi wires with different length) in both the two main directions. Table 3 summarizes the pseudoelastic groups that composed the new pseudoelastic system.

group	wires	system	length
G1	(A + B + … + *N*)	pseudoelastic parallel system with wires having the same length	l_1
G2	(a + b + … + n)	pseudoelastic parallel system with wires having same length	$l_2 < l_1$
G1 + G2	(A + B + … + N) + (a + b + … + n)	MAIN SYSTEM: pseudoelastic parallel system with wires having different length	l_1 , l_2
(G1 + G2) *and* (G1 + G2)		bi-directional device	

Table 3. Components of the bi-directional pseudoelastic device.

In order to have a symmetrical system, groups 1 and 2 have the identical number of pseudoelastic wires (i.e. N = n), and in this paper a device with N = 2 is presented.

The complex system comprises a metallic sliding shaft that is coupled to a metallic cage, see Figure 14: the shaft is free to slide through two holes formed at the two ends of the cage. In addition, three metallic disks are positioned along the shaft: the main one is fixed right in the middle of the shaft, while the others occupy an adjustable position. The distance between the fixed disk and one extremity of the cage defines the length l_1 of G1 group; besides, the distance between one adjustable disk and the same cage extremity defines the length l_2 of G2 group. According to this design, l_2 is adjustable and it is always less than l_1, and l_1 may assume only one single value. The pseudoelastic wires of G1 present a mechanical block at their ends and, in order to avoid linear buckling, all the wires are free to slide in holes prepared in the fixed metallic disk and in the extremity of the cage during the stretching of wires of G2. For the same reason, even the pseudoelastic wires of G2 group have the ends free to slide in holes prepared on the adjustable disk and on the cage. With this configuration, the wires of G2 group always deform more than do those of G1 group and the absolute stroke of the system is strictly related to the amount of deformation performed by the pseudoelastic wires of G1 and G2 groups: in particular, l_2 defines the upper limit of the stroke of the device. That is to say that the absolute stroke must not overcome the elastic limit of the stress induced martensite (SIM) of the shortest wires; in this way, it should be guaranteed a low amount of plastic deformation during cyclic. In this study, it is assumed that this limit is 8%, therefore all tests were done without overcome this limit.

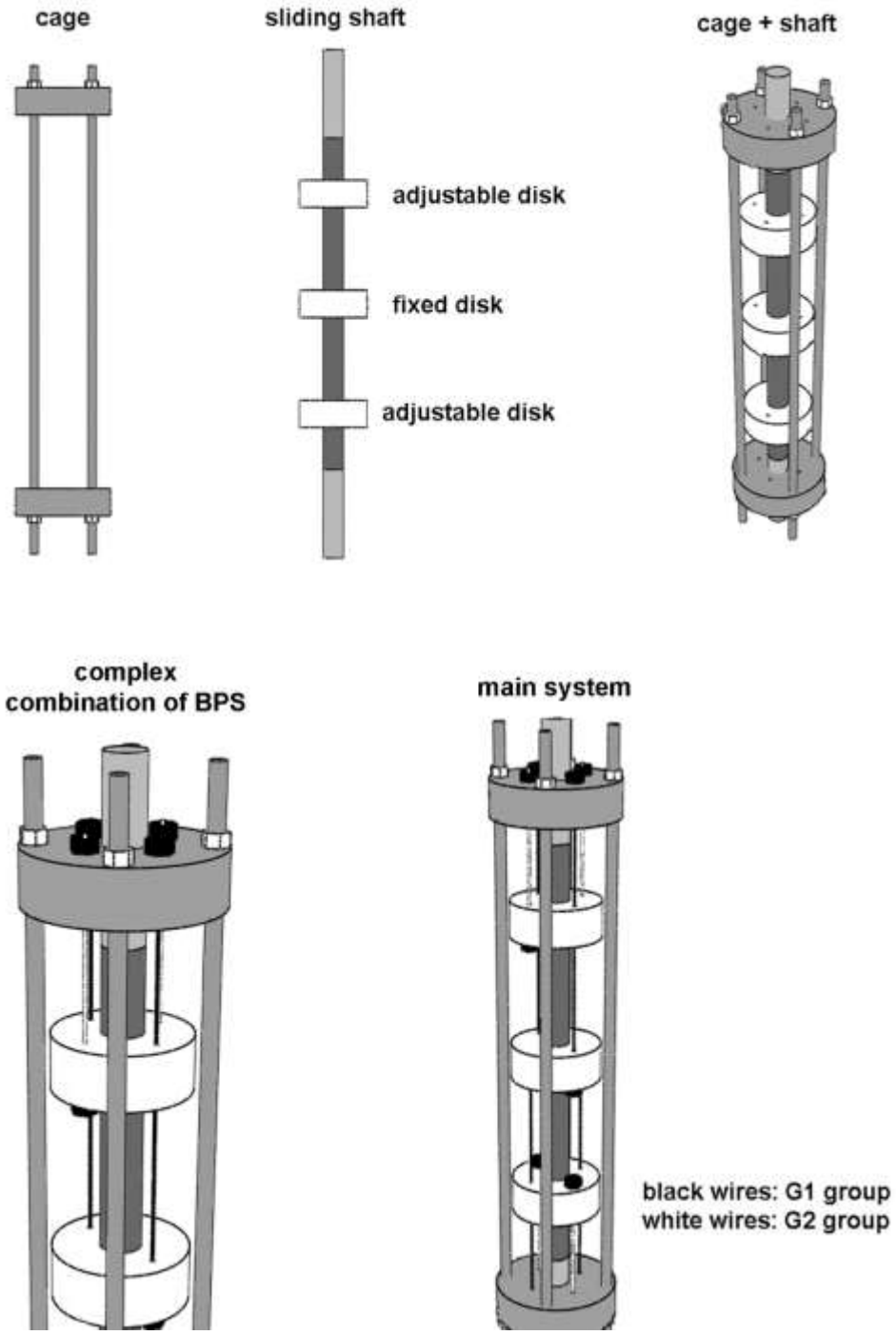

Figure 14. Components and final mounting of the complex pseudoelastic device.

The device has l_1 approximately of 169 mm while l_2 can be adjusted in the range from 60 to 125 mm. Static tests were done by standard tensile testing machine according to several values of the absolute stroke and of the maximum deformation of the pseudoelastic wires of G1 and G2 groups, see Table 4. In this table, the l_2 length, the peak-to-peak stroke and the working frequencies of the bi-directional system are reported as well. The tests were performed in the controlled deformation mode, with a deformation rate of 1%/min (calculated on l_1 length, 1.69mm/min) and following the bi-directional path.

absolute stroke [mm]	**ε_{G1} max [%]**	**ε_{G2} max [%]**	**l_2 [mm]**	**peak-to-peak stroke [mm]**	**working frequency [Hz]**
5.07	3	5	101	10.14	0.0014
5.07	3	6	84.5	10.14	0.0014
6.76	4	6	112.6	13.52	0.001
8.45	5	7	121	16.9	0.00083

Table 4. Parameters of the static tests of the complex pseudoelastic system.

Figure 15 shows the mechanical response of the bi-directional device according to the test parameters of Table 6; in the same graphs the single performance of G1 and G2 groups are reported. It can be observed that the complex system completely recovers the imposed deformation; furthermore, it shows a good stability to mechanical cyclic. The results presented in Figure 15, confirms the ones obtained for the BPS composed of two NiTi wires with different length.

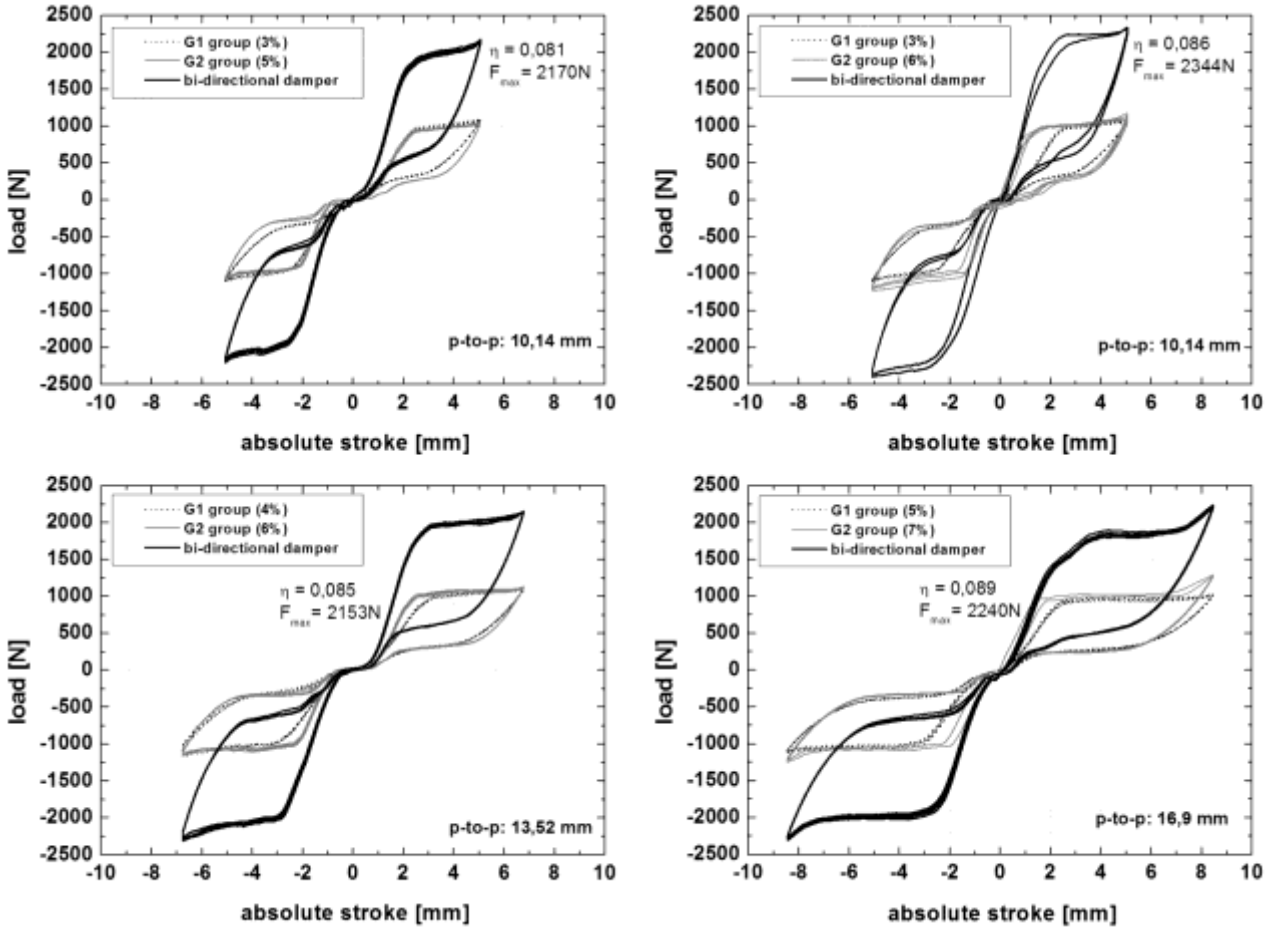

Figure 15. Mechanical response of the bi-directional system as a function of the strain ratio of the NiTi components and the peak-to-peak stroke (Black solid lines). The black dotted curves and grey solid curves represent the mechanical response of the G1 (i.e. two NiTi wire with length of 169mm) and G2 group (i.e. two NiTi wire with length *l2*, see Table 6).

4. Discussions

In this work, experimental and numerical analysis were accomplished to understand the mechanical response of complex pseudoelastic systems. Experimentation was accomplished in a static condition because the main purpose of the paper is the establishing of the functioning fundamentals of different combinations of pseudoelastic properties that at a later stage can be applied to the design of a real damper. Experimental results show that the combination of the peculiar mechanical properties of pseudoelastic materials allow to establish systems that are able to enhance and modulate the overall damping response of a SMA-based device.

There are three key parameters that best describe the performance of the proposed pseudoelastic systems referred to a complete mechanical cycle: the energy dissipated per cycle, the damping capacity and the

maximum force. As an example, Figure 16 and Figure 17 report the values of these key parameters for several combinations of NiTi wires as a function of the strain (Figure 16: case of BPS composed by two NiTi wires with the same length, Figure 17: case of BPS composed by NiTi wires with different length). It can be seen that the data reported in these pictures are coherent with those of Figure 10 and Figure 12 where single wire performance are reported. In addition, in Figure 16 and Figure 17 it can be seen that the experimental damping capacity of a NiTi system increases with the increasing of the maximum strain of the single NiTi component until a maximum value of approximately 0.09. In addition, it is evident that the energy dissipated per cycle and the maximum force are both strictly related to the strain. In fact, as an example, two NiTi wires with the same length dissipate 681 Nmm per cycle when work at 4% of maximum strain and reach a maximum force of 972N. When one of this wire is substituted with a shorter one (see the last combination of Figure 17), a maximum force of 1076 N is registered and the resulting system dissipates higher energy per cycle (1412 Nmm) with respect to the previous case. This improvement is related to the shortest wire which starts to transform into SIM earlier than the coupled longest wire (the one that works at 4%); therefore, at the same absolute stroke, the amount of dissipate energy of the shortest wire is higher than the one registered for longest wire. In addition, a significant increase of the maximum force can be observed, and, as expected, the resulting maximum force is proportional to the number of NiTi wires.

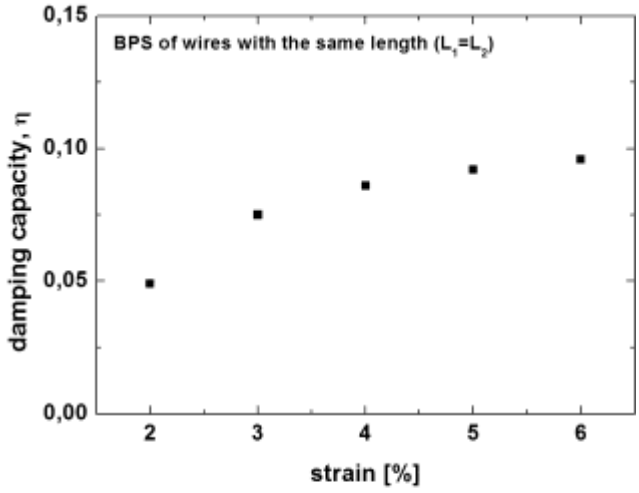

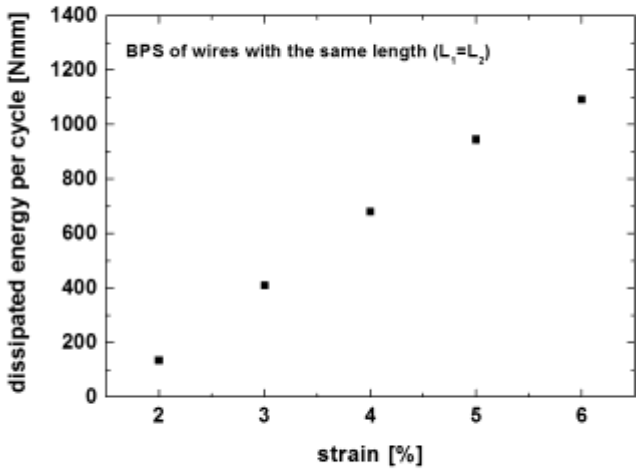

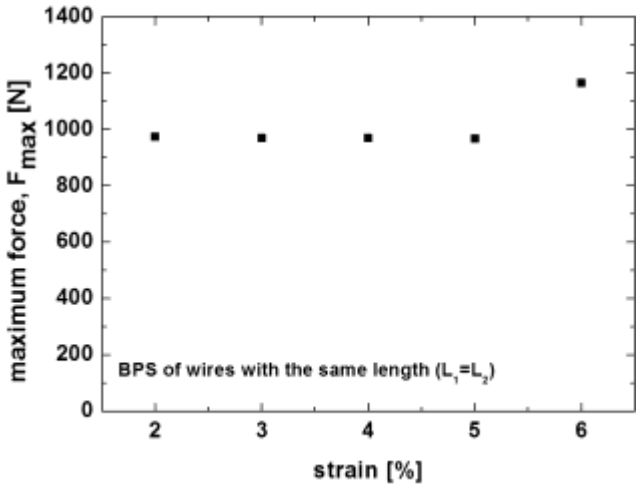

Figure 16. Damping capacity, energy dissipated per cycle and maximum force at different strain of the BPS composed of two NiTi wires with the same length.

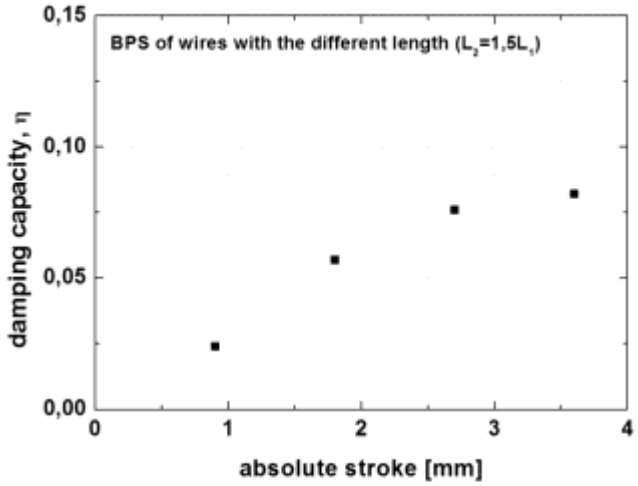

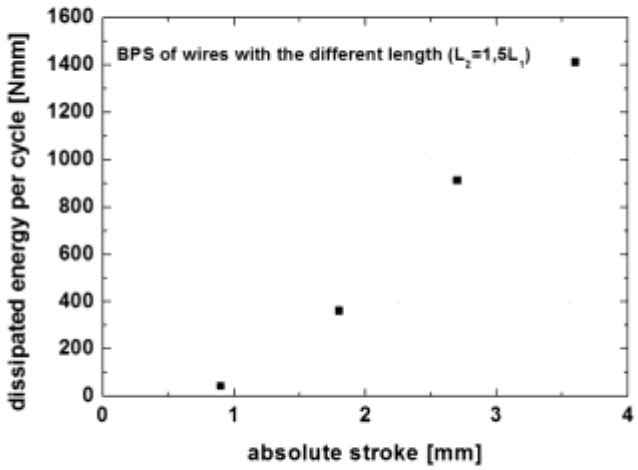

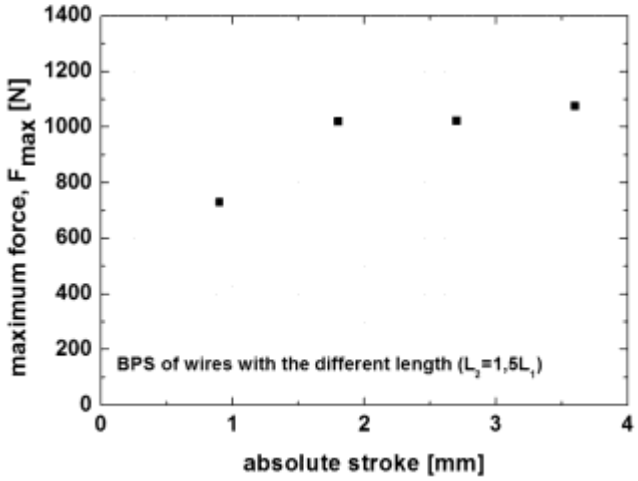

Figure 17. Damping capacity, energy dissipated per cycle and maximum force at different strains of the BPS composed of two NiTi wires with the different length.

The proposed numerical model confirms experimental results. As an example, Figure 18 and Table 5 show the numerical simulations of wire pairs, both with same and different length. Considering experimental and numerical results of 4%+6% coupling (Figure 17 and Table 5) it can be seen that both the dissipated energy and the damping capacity are well modeled. Besides, as observed in experimentations, the model shows that the strain is the most relevant parameter; as an example, the coupling of two 90 mm long wires, which reach both the 6% is more efficient than a wire 90 mm long working at 3% coupled to one 45 mm long working at 6%. In addition, from data of Table 5, it can be also seen that the model confirms 0.09 as the upper limit of the damping capacity of any complex pseudoelastic system composed of NiTi wires with arbitrary length.

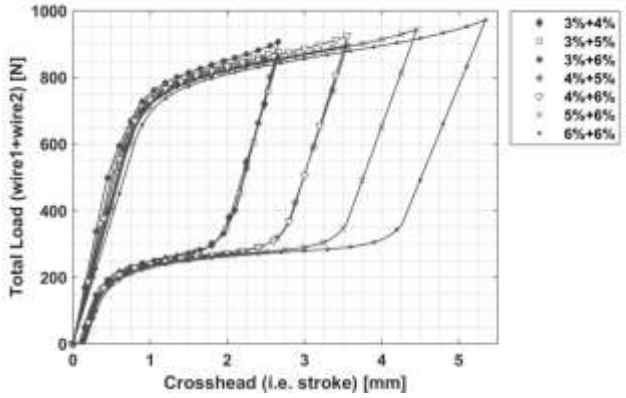

Figure 18. Examples of simulations of wire pairs, both with same length and different length.

L2/L1	Coupling	Dissipated energy [Nmm]	Stored energy [Nmm]	Damping capacity η
1.3	**3%+4%**	932	1755	0.0845
1.67	**3%+5%**	982	1812	0.0862
2	**3%+6%**	1015	1861	0.0869
1.25	**4%+5%**	1408	2525	0.0887
1.5	**4%+6%**	1453	2590	0.0893
1.2	**5%+6%**	1897	3335	0.0905
1	**6%+6%**	2341	4102	0.0908

Table 5. Damping capacity, dissipated and stored energies at different strain by the numerical simulations of coupling of wires with length L1 and L2.

Furthermore, it is worth highlight that the coupling of two wires with different length allow one more “intrinsic” result: that is the modulation of the elastic response. This is due to the lag time between the beginning of SIM of the two wires (as the short wire detwins first), allowing both a change of stiffness and an enlargement of the elastic region. In this way, the elastic region may further change (in force and/or in stroke) if more than two wires are coupled, and in this case the elastic region will show more than two changes of stiffness and, consequently, the final SIM may delay due to the new intermediate elastic parts.
The possibility to combine more than two wires to investigate the modulation of the elastic region is numerically explored with the two examples in Figures 19 and 20. The coupling of three wires, in the first case two of which have the same strain, is plotted and, to highlight the changes in the loading path, the derivative with respect to the stroke is overlapped. Coupling wires with high difference of strains produce a greater fall in the load slope, while using closer strains allows splitting more the region before the plateau. However, the combination of pseudoelastic wires with different length may enable a short fatigue life of the shortest wire; to overcome this limit, the final system should be designed to not overcome a strain limit that is defined according to the length of the shortest wire. Usually, pseudoelastic materials are strained up to a partial elastic deformation of the stress induced martensite (approximately 8-10% [1, 3]), as higher strains may cause firstly plasticity of martensite and then fracture of the material.

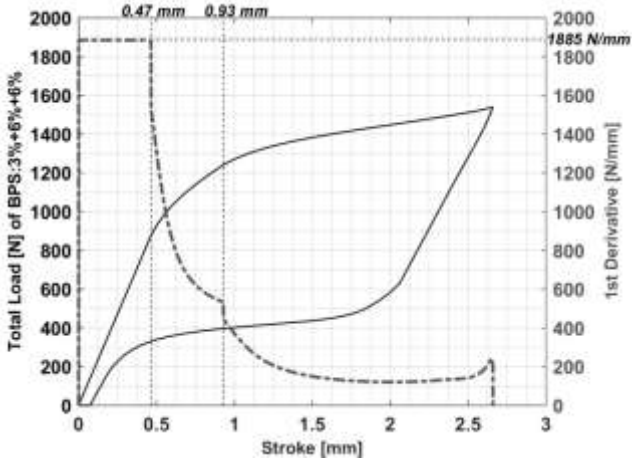

Figure 19. Simulations of the coupling of three wires at 3%, 6% and 6%. Solid line is the Load; dashed one is its derivative (loading only) with respect to stroke.

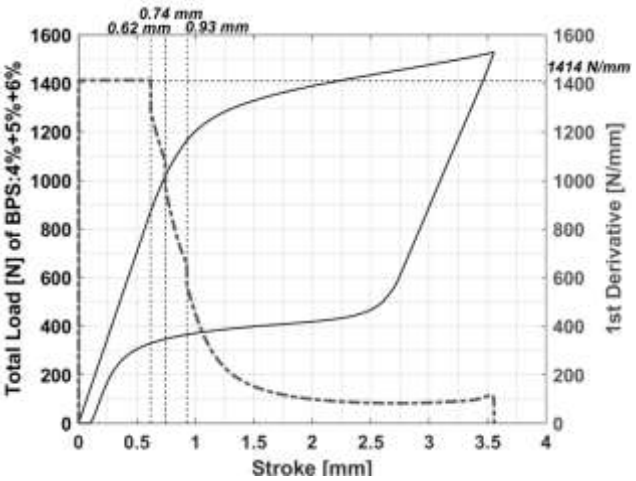

Figure 20. Simulations of the coupling of three wires at 3%, 4% and 5%. Solid line is the Load; dashed one is its derivative (loading only) with respect to stroke.

Furthermore, as expected, groups of pseudoelastic wires allows improvements both in the expressed force and in the energy dissipated per cycle (Table 6). Moreover, the use of groups of wires with different length may produce, besides the modulation of the elastic region, also the adaptability to critical events. For instance, in case of the shortest wires break to unexpected large strains, or in case they reach a maximum strain, the longest wires would continue working and therefore the damping response will be ever guaranteed.

strain of bi-directional system (two groups of NiTi wires) [%]	**damping capacity**	**energy dissipated per cycle [Nmm]**	**Fmax [N]**
group 1: 3% group 2: 5%	0.081	3855	2170
group 1: 3% group 2: 6%	0.086	4639	2344
group 1: 4% group 2: 6%	0.085	5550	2153
group 1: 5% group 2: 7%	0.089	7461	2240

Table 6. Damping capacity, energy dissipated per cycle and maximum force at different strain of the pseudoelastic system composed of two groups of NiTi wires with different length.

Besides, the pseudoelastic system follows the principal requirements of a generic damper [12]: its length remains invariant during functioning; since tests were accomplished in quasi-static conditions, the self-heating can be neglected; it promotes the re-centering with the complete return to the start position and bi-directionality. Further requirements proposed in [12] (as fatigue life, daily temperature, direct rain) are not general conditions but they belong to a specific event (quakes or stayed cables) and lie outside the purpose of the present study.

Finally, the presented results are based on few combinations of pseudoelastic wires, but they are the starting point of a wide range of any further possible combinations that can be implemented to damp different kinds of events. By doing this, it is evident that a numerical approach can be useful in detecting the great part of these possible combinations. As said in Section 3.2, the result of the coupling of parallel wires can be obtained as a linear combination of the single wires taken individually. Therefore, once the model is tuned on the individual wires, it is possible to simulate any type of combination, so to use the model as a predictive tool to perform a parametric optimization. As an example, Figure 21 shows the numerical simulation of a pseudoelastic system based on two groups of NiTi wires each composed of four pseudoelastic wires and one group performing at 4% and the other at 6% of strain (l1 = 90mm, l2 = 60mm).

The simulations in Figures from 18 to 21 are just a sample of the studies that can be done with a predictive purpose. However, in this paper we mainly reported the cases of validation, useful to prove the efficiency of the model itself, while simulations that are more extensive and the development of a parametric optimization on damping capacity are sent back to the case of a particular application, with specific project requirements of strength and energy.

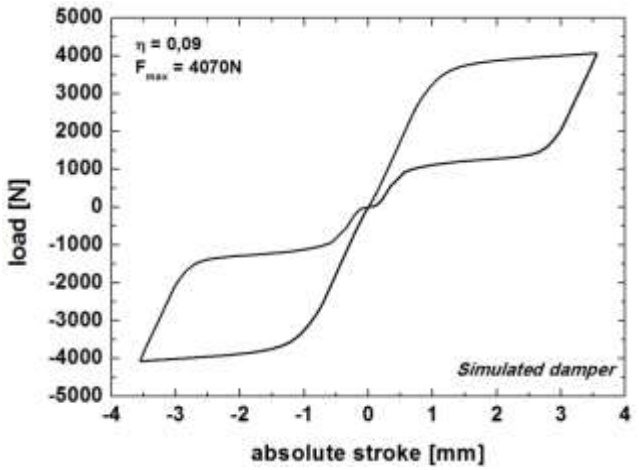

Figure 21. Numerical simulation of an articulated pseudoelastic system, composed of two groups of NiTi wire (four wires each group) one performing at 4% (l_1 = 90mm) and the other at 6% (l_2 = 60mm).

5. Conclusion

This work presents a deep experimental study on the improvement and modulation of the quasi-static pseudoelastic response of SMA. It was found that any system composed of NiTi wires presents an upper limit of the damping capacity (approximately 0.09). Furthermore, it was observed that the coupling of NiTi wires with different length can modulated the elastic response of the system. Because of the large number of different kinds of events, a large variety of damping systems are required, with forces and strain calibrated on the specific situation; therefore, a numerical model was proposed to solve any kind of force/strain requirement. With respect to the model, it was presented how to tune the simulation results by changing the argument of the logarithm of the sigmoid function used to represent the kinetics. In this way, it was possible to model the behavior of the rhombohedral phase, taking care to add to stress and temperature, the deformation as a control variable.

Nomenclature

η	Loss factor
E'	Storage modulus
E''	Loss modulus
W_d	Energy dissipation per cycle
W_e	Stored energy during loading
E_A, E_M, E_R	Young modulus of austenite, martensite and rhombohedral
ξ_A, ξ_M, ξ_R	Phase volumetric fraction of austenite, martensite and rhombohedral
ρ_0	Density
ε_L	Maximum strain due to SIM detwinning
L_h	Latent heat
T_{cr}	Thermodynamic transformation temperature
C_p	Specific heat
T_0	Ambient or reference temperature
α	Thermal dilatation coefficient.
V	Volume
C_X	Clausius-Clapeyron coefficient of the transformation that has the phase 'X' as product phase
T_{PX}, T_{SX}, T_{FX}	Peak, start and finish temperatures for the transformation 'X'
ξ_X	Phase volumetric fraction of the 'X' phase

Acknowledgments

Authors are grateful to Mr. Enrico Bassani of CNR IENI (Lecco Unit) for the precious technical assistance.

References

[1] Otsuka K, Ren X. Physical metallurgy of Ti–Ni-based shape memory alloys. Prog Mate Sci 2005; 50:511–678

[2] Nespoli A, Biffi CA, Casati R, Villa E, Tuissi A, Passaretti F. New Developments on Mini/Micro Shape Memory Actuators, in Smart Actuation and Sensing Systems—Recent Advances and Future Challenges, G. Berselli, R. Vertechy, and G. Vassura, Ed., ISBN 978-953-51-0798-9

[3] Treadway J, Abolmaali A, Lu F, Aswath P. Tensile and fatigue behavior of superelastic shape memory rods. Materials and Design 2015; 86:105–113

[4] Jani JM, Leary M, Subic A, Gibson MA. A review of shape memory alloy research, applications and opportunities. Mater Des 2014; 56:1078–1113

[5] Nespoli A, Rigamonti D, Villa E, Passaretti F. Design, characterization and perspectives of shape memory alloy elements in miniature sensor proof of concept. Sens Actuators 2014; 218:142–153

[6] Borlandelli E, Scarselli D, Nespoli A, Rigamonti D, Bettini P, Morandini M, Villa E, Sala G, Quadrio M. Design and experimental characterization of a NiTi-based, high-frequency, centripetal peristaltic actuator. Smart Mater Struct 2015; 24:035008

[7] Auricchio F, Boatti E, Conti M. SMA Biomedical Applications, pages 307-341, in L. Lecce and A. Concilio editors, in “Shape Memory Alloy Engineering for Aerospace, Structural and Biomedical Applications”, Elsevier 2015

[8] Nespoli A, Dallolio V, Stortiero F, Besseghini S, Passaretti F, Villa E. Design and thermo-mechanical analysis of a new NiTi shape memory alloy fixing clip. Mater Sci Eng C 2014; 37:171–176

[9] Nespoli A, Dallolio V, Villa E, Passaretti F. A new design of a Nitinol ring-like wire for suturing in deep surgical field. Mater Sci Eng C 2015; 56:30–36

[10] Ozbulut OE, Hurlebaus S, Desroches R. Seismic Response Control Using Shape Memory Alloys: A Review. J Intel Mater Syst Struct 2011; 22:1531-1549

[11] Gholampour AA, Ghassemieh M, Kiani J. State of the art in nonlinear dynamic analysis of smart structures with SMA members. Int J Eng Sci 2014; 75:108-117

[12] V. Torra, A. Isalgue, F.C. Lovey, M. Sade, Shape memory alloys as an effective tool to damp vibrations. Study of the fundamental parameters required to guarantee technological applications, J. Therm Anal. Calorim (2015) 119:1475-1533

[13] C. V. Suciu, T. Tobiishi, R. Mouri, Modeling and Simulation of a Vehicle Suspension with Variable Damping versus the Excitation Frequency, J. of telecommunication and information technologies 1/2012, 83-89

[14] R.C.V. Loureiro, J. M. Belda-Lois, E. R. Lima, J. L. Pons, J. J. Sanchez-Lacuesta, W. S. Harwin, Upper Limb Tremor Suppression in ADL via an Orthosis Incorporating a Controllable Double Viscous Beam Actuator, Proceedings of the 2005 IEEE
9th International Conference on Rehabilitation Robotics June 28 - July 1, 2005, Chicago, IL, USA

[15] Z. Ilic, B. Rasuo, M. Jovanovic, S. Pekmezovic, A. Bengin, M. Dinulovic, Potential connections of cockpit floor seat on passive vibration reduction at a piston propelled airplane, Tehnički vjesnik 21, 3(2014), 471-478].

[16] Indirli M, Castellano MG. Shape memory alloy devices for the structural improvement of masonry heritage structures. Int J Arch Heritage 2008; 2:93-119

[17] Ren W, Li H, Song G. An innovative shape memory alloy damper for passive control of structures subjected to seismic excitations, Proc. 14th World Conference on Earthquake Engineering, 2008, Beijing, China

[18] Fischer FD, Tanaka K. A Micromechanical Model for the Kinetics of Martensitic Transformation. Int J Solids Struct 1992; 29:1723-1728

[19] Raniecki B, Lexcellent C, Tanaka K. Thermodynamic Model of Pseudoelastic Behavior of Shape Memory Alloys. Arch Mech 1992; 44:261-284

[20] Bernardini D. Models of hysteresis in the framework of the thermomechanics with internal variables. Physica B 2001; 306:132-136

[21] Tanaka K. A thermomechanical sketch of shape memory effect: One-dimensional tensile behavior. Res Mechanica 1986; 18:251–263

[22] Liang C, Rogers CA. One-Dimensional Thermomechanical Constitutive Relations for Shape Memory Materials. J Intell Mater Syst Struct 1990; 1:207-234

[23] Brinson LC. One-Dimensional Constitutive Behavior of Shape Memory Alloys: Thermomechanical Derivation with Non-Constant Material Functions and Redefined Martensite Internal Variable. J Intell Mater Syst Struct 1993; 4:229-242

[24] Auricchio F, Sacco E. A temperature-dependent beam for shape-memory alloys: Constitutive modelling, finite-element implementation and numerical simulations Comp Meth Appl Mech Eng 1999; 174:171-190

[25] Popov P, Lagoudas DC. A 3-D constitutive model for shape memory alloys incorporating pseudoelasticity and detwinning of self-accommodated martensite. Intern J Plast 2007. 23:1679-1720

[26] Müller I, Seelecke S. Thermodynamic aspects of shape memory alloys. Mathem Comp Mod 2001; 34:1307-1355

[27] Auricchio F, Petrini L. A three-dimensional model describing stress-temperature induced solid phase transformations: solution algorithm and boundary value problems. Intern J Num Meth Eng 2004; 61:807-836

[28] Zhu S, Zhang Y. A thermomechanical constitutive model for superelastic SMA wire with strain-rate dependence. Smart Mater Struct 2007; 16:1696-1707

[29] Helbert G, Saint-Sulpice L, Chirani SA, Dieng L, Lecompte T, Calloch S, Pilvin P. Experimental characterisation of three-phase NiTi wires under tension. Mechanics of Materials 2014; 79: 85-101

[30] Sedlak P, Frost M, Benesova B, Ben Zineb T, Sittner P. Thermomechanical model for NiTi-based shape memory alloys including R-phase and material anisotropy under multi-axial loadings. International Journal of Plasticity 2012; 39: 132-151

[31] Chan CW, Chan SHJ, Man HC, Ji P. 1-D constitutive model for evolution of stress-induced R-phase and localized Luders-like stress-induced martensitic transformation of super-elastic NiTi wires. International Journal of Plasticity 2012; 32-33: 85-105

[32] Olbricht J, Yawny A, Pelegrina JL, Dlouhy A, Eggeler G. On the Stress-Induced Formation of R-Phase in Ultra-Fine-Grained Ni-Rich NiTi Shape Memory Alloys. Metallurgical and Materials Transactions A-Physical Metallurgy and Materials Science 2011; 42A,9: 2556-2574

[33] Duerig TW, Bhattacharya K. The Influence of the R-Phase on the Superelastic Behavior of NiTi. Shape Memory and Superelasticity 2015; 1: 153-161

[34] Nespoli A, Passaretti F, Villa E. Phase transition and mechanical damping properties: A DMTA study of NiTiCu shape memory alloys. Intermetal 2013; 32:394-400

[35] Carfagni M, Lenzi E, Pierini M. The loss factor as a measure of mechanical damping, Conference: 1998 IMAC XVI - 16th International Modal Analysis Conference

[36] Wang X, Kustov S, Verlinden B, Van Humbeeck J. Fundamental Development on Utilizing the R-phase Transformation in NiTi Shape Memory Alloys. Shap Mem Superelasticity DOI 10.1007/s40830-015-0007-2